Journal of Materials Chemistry A

ROYAL SOCIETY OF CHEMISTRY

PAPER

View Article Online
View Journal | View Issue

Check for updates

Cite this: J. Mater. Chem. A, 2026, 14, 16840

Benchmarking *operando* neutron diffraction for high-power Li-ion batteries

Dat Le Thanh, [abc] Claire Villevieille, [d] Romain Berthelot *[be] and Emmanuelle Suard *[a]

Received 22nd December 2025
Accepted 6th March 2026

DOI: 10.1039/d5ta10422j

rsc.li/materials-a

Neutron powder diffraction is a powerful method for probing structural changes and localizing and quantifying lithium in battery electrode materials, but acquiring high-quality patterns during *operando* type measurement remains challenging due to the need for both good electrochemistry and a large active material amount for an optimal signal-to-noise ratio. However, this technique is rarely applied during fast cycling of high-rate electrode materials despite the growing demands of high-power batteries. Herein, we benchmarked two cell designs for *operando* measurement, coin-type and cylindrical cells, on two different diffractometers (high-resolution and high-flux instruments) using high-rate Wadsley–Roth $FeNb_{11}O_{29}$ as a model electrode material. The coin-type cell provides an excellent signal-to-noise ratio and ease of assembly, yet it relies on deuterated electrolytes. In contrast, a cylindrical cell delivers reliable electrochemistry at fast cycling rates while still providing neutron diffraction data of sufficient quality for structural analysis even when using conventional organic electrolyte. The two diffractometers also exhibit complementary capability: the high-flux instrument enabled fast data acquisitions in only a few minutes, while the high-resolution one was successfully employed in *in situ* mode for the first time with clearer peak separation. These results validate the cylindrical cell as a promising setup for realistic, high-rate cycling, paving the way towards more accessible and cost-effective *operando* neutron studies in battery research.

1. Introduction

Li-ion batteries (LIBs) have revolutionized energy storage, powered portable electronics and electric vehicles, and enabled grid-scale applications.[1–6] Continuous improvement of their electrochemical performance, safety, and lifetime is heavily based on advanced characterization techniques that reveal the structural, physicochemical, and electrochemical properties of both newly developed and well-established electrode materials. Among these, *in situ* and *operando* methods have become indispensable for tracking structural evolution inside working cells while avoiding exposure to air or moisture. *Operando* techniques, in particular, enable real-time observation of metastable phases and dynamic, out-of-equilibrium processes during cycling, which offer comprehensive insights into battery reaction mechanisms.

Among different characterisation methods, neutron powder diffraction (NPD) is a powerful technique in battery research owing to several advantages presented hereafter. First, it is particularly sensitive to light elements (*e.g.* lithium and oxygen) and can distinguish neighbouring elements (*e.g.* nickel, manganese, and cobalt in layered oxides), thanks to the irregular variations in neutron scattering lengths across the periodic table. Besides, due to their weak interaction with atom nuclei, neutrons are non-destructive and exhibit penetration depths that are much larger than those of X-rays, allowing for the bulk analysis of entire electrodes or even full batteries. Additionally, neutron scattering lengths are independent of the scattering vector Q, providing strong signal intensity even in high Q regions for accurate determination of structural parameters such as site occupancies and Debye–Waller factors. These advantages have motivated the development of *in situ* and *operando* NPD over the past three decades to address its stringent experimental requirements. Reliable measurements require both homogeneous electrochemical reactions and a large amount of active material to achieve an adequate diffraction signal while minimizing parasitic scattering from other cell components. Lithium-ion batteries contain several elements problematic for NPD: metallic parts such as current collectors or casings contribute intense Bragg peaks, while natural lithium strongly absorbs neutrons. Additionally, conventional organic-based electrolytes and separators are usually rich in hydrogens, whose incoherent cross section far exceeds its coherent value (σ_{inc} = 80.27 barns *vs.* σ_{coh} = 1.75 barns), resulting in

[a]Institut Laue-Langevin (ILL), 38042, Grenoble, France. E-mail: suard@ill.fr
[b]ICGM, Université de Montpellier, CNRS, ENSCM, 34095, Montpellier, France. E-mail: romain.berthelot@umontpellier.fr
[c]Alistore-European Research Institute, CNRS FR 3104, 80039, Amiens, France
[d]Univ. Grenoble Alpes, Univ. Savoie Mont Blanc, CNRS, Grenoble INP, LEPMI, Grenoble, 38000, France
[e]Réseau sur le Stockage Électrochimique de l'Énergie (RS2E), CNRS, 80039, Amiens, France

a featureless background that substantially lowers the diffraction pattern's signal-to-noise ratio. Although this can be mitigated by using deuterated electrolytes and low-hydrogen materials, deuteration is costly. Furthermore, the flux of neutron sources is several orders of magnitude lower than that of X-ray facilities, and neutron scattering cross-sections are smaller, necessitating large sample quantity and long acquisition times for good counting statistics. Consequently, only a few neutron facilities worldwide currently provide the flux and resolution required for *operando* NPD investigations of battery materials.

The development of custom-designed electrochemical cells became essential for *in situ* and *operando* NPD experiments. The central challenge in such designs has always been balancing the two conflicting requirements: ensuring sufficient loading for proper neutron signals while maintaining good electrochemical performance. Since the first custom-made cells were introduced in 1998,[7,8] several cell designs have been developed and can be divided into three main categories: coin-type, pouch-type, and cylindrical roll-over cells[9–29] (Note S1 and Fig. S1).

Despite these advances, further progress is challenging due to the trade-off between data quality and electrochemical performance. Existing cylindrical cells are based on costly deuterated electrolytes and long acquisition times, while coin-type cells suffer from thick electrodes and slow kinetics. To overcome these challenges, in this work a custom-designed cylindrical cell was developed combining advantages of several features such as (i) a neutron transparent body based on a Ti–Zr alloy ($\sim Ti_{2.08}Zr$)[30] used as a cell casing, (ii) a rolling approach ensuring high loaded electrodes, ideal for temporal resolution, and (iii) a double coated electrode ensuring good electrochemical performance even at fast cycling rates. Niobium-based oxide $FeNb_{11}O_{29}$ was chosen as a model electrode material to validate this cell configuration. Indeed, $FeNb_{11}O_{29}$ belongs to the family of Wadsley–Roth oxides, known to exhibit excellent rate capability, and is currently intensively investigated as a promising alternative to negative electrodes in future LIBs.[31–43]

In this work, we aim to benchmark complementary instruments and cell designs for *in situ*/*operando* NPD: (i) two diffractometers at the Institut Laue-Langevin (high-resolution D2B and high-flux D20) and (ii) two NPD cell designs, the reported coin-type cell and a newly developed cylindrical cell. Overall, this work explores three key opportunities: (i) extending the D2B diffractometer's capabilities to perform *in situ* experiments, (ii) enabling reliable electrochemical cell cycling at higher rates while collecting neutron diffraction patterns, and (iii) demonstrating the practicality of using standard electrolytes. The study begins by introducing the two cell designs and component choices, then compares their electrochemical performance and evaluates how each component contributes to NPD data and finally focuses on *operando* data analyses on both cells and diffractometers. Together, these objectives aim to identify the prospects and challenges for making *in situ* and *operando* NPD studies more accessible, cost-effective, and closer to routine application in battery research, while still retaining good electrochemical cycling and sufficient data quality.

2. Experimental

2.1. Material synthesis and electrode preparation

Monoclinic $FeNb_{11}O_{29}$ was synthesized by a solid-state reaction at 1100 °C in 4 h from a stoichiometric mixture of Fe_2O_3 (≥99%, <5 μm, Honeywell) and Nb_2O_5 (obtained by heating Nb powder (99.8%, ~325 mesh, Alfa Aesar) at 900 °C for 24 h). Its phase purity was verified by X-ray diffraction (Fig. S2).

For the coin-type cell, a self-standing electrode was prepared by grinding $FeNb_{11}O_{29}$, carbon super P (Alfa Aesar) and a poly(tetrafluoroethene) (PTFE, Sigma-Aldrich) binder in an 80 : 10 : 10 weight ratio, followed by pressing the mixture into a ~1 mm thick pellet (~400 mg in total, ~127 mg cm^{-2}).

For the cylindrical cell, a double-coated electrode on Cu foil with a high mass loading (~20 mg cm^{-2}) was prepared from $FeNb_{11}O_{29}$, carbon Super P (Alfa Aesar), and a PVDF binder (Solef® 5130) in a 90 : 5 : 5 weight ratio. Around 3 g of dry mixture was mixed, dispersed in ~3.5 mL of *N*-methyl-2-pyrrolidone (NMP, Sigma-Aldrich, 99.5%) (~45% dry mass), homogenized in a Kakuhunter planetary centrifugal mixer (SK-300SII) and then coated onto 20 μm Cu foil (Goodfellow) using a 0.4 mm doctor-blade gap. The coated foil was air-dried for 2 hours to prevent cracking and adhesion issues, followed by vacuum drying at 80 °C for 12 hours before coating the opposite side. The composite electrode was then calendared to a targeted porosity of ~44% to optimize porosity and ensure uniform thickness and lastly cut to 5.5 × 20 cm. The total mass of active material $FeN_{11}O_{29}$ is estimated to be ~4 g.

2.2. Cell assembly

For the coin-type cell, the self-standing electrode was paired with metallic lithium (Sigma-Aldrich) as the counter electrode, separated by a Whatman glass fiber separator impregnated with 0.4 mL of deuterated electrolyte (1 M $LiPF_6$ in d-EC/d-DMC, 1 : 1 by volume, Solvionic).

The cylindrical cell was assembled as illustrated in Note S2 and Fig. S3. The double-coated $FeN_{11}O_{29}$ electrode was paired with Li foil supported on a Cu grid as the counter/reference electrode, separated by two layers of a Celgard separator. The complete stack (electrode/separator/Li/separator) was carefully and tightly rolled around the central $Ti_{2.08}Zr$ rod, ensuring proper alignment and no short-circuiting. Finally, 2 mL of conventional organic electrolyte (1 M $LiPF_6$ in EC/DMC, 3 : 7 by volume) was uniformly added for complete wetting.

Constraints of the cells and research objectives governed the choice of electrolyte. Indeed, a deuterated electrolyte was used for the coin-type cell, to minimize incoherent scattering and ensure sufficient data quality despite low active material mass loading. Conversely, the cylindrical cell was filled with conventional electrolyte to demonstrate the feasibility of practical, cost-effective cycling conditions. Both electrolytes were reported to exhibit comparable electrochemical signatures and stability,[21] supporting the comparability between the two designs.

For comparison, a CR2032 coin cell was assembled using a single-side coated $FeNb_{11}O_{29}$ electrode (~20 mg cm^{-2}),

a lithium counter electrode, and a Whatman glass fibre separator impregnated with 0.1 mL of the same conventional organic electrolyte. The cell was cycled at a current rate of C/12 between 1.0 and 3.0 V *vs.* Li^+/Li. The nominal specific capacity C is defined as one electron transfer per transition metal ($Fe^{3+/2+}$ and $Nb^{5+/4+}$ redox couples), corresponding to 12 Li^+ per formula unit or ~209 mA h g^{-1}, although the subsequent reduction of Nb^{4+} to Nb^{3+} could result in extra capacity.[31–43] Throughout the manuscript, all the potentials will be expressed *vs.* the Li metal counter electrode so *vs.* Li^+/Li.

2.3. *Operando* NPD experiments

NPD data of the coin-type cell were collected at the D20 beamline, with a pattern acquired every 15 minutes while the cell was cycled at a C/36 rate between 0.8 V and 3.0 V *vs.* Li^+/Li.

The cylindrical cell was tested using both D2B and D20 diffractometers (Fig. S4). NPD measurements were first performed on individual components of the cylindrical cell to assess their contributions: pristine $FeNb_{11}O_{29}$ powder, the electrode coated on Cu foil, and the assembled cell before and after electrolyte filling. These reference data were collected on both D2B and D20 instruments, with acquisition times of 2 h and 5 min, respectively.

On the D2B diffractometer, the first discharge of the cylindrical cell followed a sequence of 2 h at C/12 (1 Li^+ per h, 17.38 mA g^{-1}) and 6 h of rest for NPD acquisition. This sequence was repeated five times to reach specific $Li_xFeNb_{11}O_{29}$ compositions ($x = 0, 2, 4, 6, 8, 10$). The subsequent delithiation (charge) was performed outside the D2B diffractometer to restore the cell to its initial state before further measurements on the D20 diffractometer.

On the D20, NPD patterns were collected every 5 minutes throughout three discharge–charge cycles at C/12, C/6 and C/2 rates; during each 5-minute acquisition, these current values correspond to Li^+ insertion/extraction rates of 1/12, 1/6 and 1/2 Li^+ per $FeNb_{11}O_{29}$ formula unit, respectively. The first discharge process was conducted stepwise through 11 sequences, each comprising 1 h of discharge at a C/12 rate followed by 1 h of rest for long NPD acquisition of $Li_xFeNb_{11}O_{29}$ compositions ($x = 0$–11). At the end of the first discharge, the cell was charged at C/12 to the initial state. Then, two further cycles were conducted, each consisting of a galvanostatic cycling step at higher rates (C/6 and C/2), followed by a 30-minute constant-voltage hold at the end of discharge and charge to ensure complete reaction.

2.4. Data analysis

For each set of NPD data collected in the same configuration and using the same instrument, the patterns exhibited consistent background features. Therefore, a point-by-point interpolated background function was used for each dataset and applied for background subtraction. Rietveld refinements of the NPD patterns were collected using the FullProf Suite package.[44] For data obtained with the coin-type cell, only the $FeNb_{11}O_{29}$ active material phase was observed and thus considered in the refinement. By contrast, the patterns collected with the cylindrical cell contained three contributions: $FeNb_{11}O_{29}$ (refined by the Rietveld method) and the Cu current collector and Li counter electrode, both of which were refined using the Le Bail method (profile matching with fixed scale factors). The validity of Le Bail refinements was justified as the two additional phases (Cu and Li) have little overlap with the main phase.

For Cu and Li, zero shift and cell parameters were refined for the first pattern in each series and subsequently fixed for all subsequent refinements. For lithiated $FeNb_{11}O_{29}$, the refined parameters included the lattice constants (a, b, c, and β), scale factor, and overall B factor; atomic positions and individual isotropic displacement parameters were not refined. Due to the structural complexity, with 12 crystallographic Li sites (Fig. S5 and Table S1) and the low Li content relative to other atoms, which is typical of Wadsley–Roth phases, localizing Li is challenging. This difficulty was reflected in the literature: while chemically lithiated phases have been analysed using NPD on high crystallinity powders,[45] no NPD studies have been reported for electrochemically lithiated samples. Attempted refinement strategies, such as constraining Li to specific sites (only horizontal/vertical windows or pocket sites) or excluding it entirely, yielded negligible changes in cell parameters (<0.1%) and little improvement in fit quality. Therefore, a different approach was used: the Li amount of each lithiated composition is equally distributed over all 12 sites (equal Li site occupancies).

3. Results and discussion

3.1. Comparison of the two cell designs

The two cell designs examined in this work present pros and cons that are necessary to discuss. On the one hand, the coin-type cell combines a neutron-transparent body with hydrogen-free components (deuterated electrolytes and glass fibre separators) and efficient use of active materials (~200 mg), as shown in Fig. S1.[21] These features provide stable electrochemistry at moderate current rates (C/4 for 19 mg and C/24 for 200 mg electrodes), while delivering sufficient counting statistics for reliable Rietveld structural refinements. This is a typical design to answer questions related to pure fundamental investigation for short term cycling experiments.

On the other hand, the cylindrical cell[29] provides maximum data quality while providing long-term cycling capability (Fig. 1 and S3). The same "null-matrix" alloy was used for the cell body and central rod was used as a current collector. The cell body is a hollow cylinder that houses a "jelly-roll" electrode assembly. The central rod consists of two parts: (i) a longer rod in direct contact with the positive electrode foil and (ii) a shorter rod, connected to the negative electrode by a current tab; these two rods are separated by an insulating part made of polyetheretherketone (PEEK). Owing to its chemical stability and mechanical strength, PEEK is also used for the sealing caps, ensuring that the cell remains airtight.

Regarding cylindrical cell components, Celgard 2500 was selected as a separator due to its high tensile strength, resistance to tear and puncture, decent flexibility, and good ion transport properties. Despite its hydrogen content, which causes incoherent scattering, it remains the best compromise among tested materials (Celgard, PVDF, polyethylene, and PET/alumina

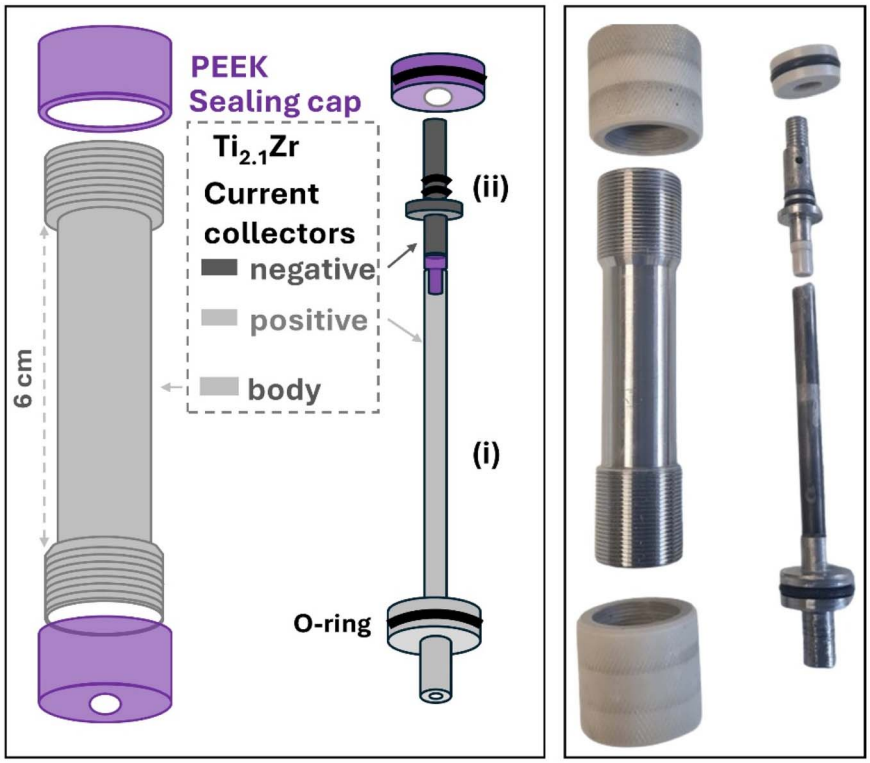

Fig. 1 Illustration of the cylindrical NPD cell and its photograph.

composites).[29] The current collector is copper mesh and foil, preferred over aluminium to avoid Li–Al alloying and minimize peak overlap with $FeNb_{11}O_{29}$. Pieces of lithium foil were flattened to low thickness (~200 μm) to reduce neutron absorption and improve interfacial contact, lowering the cell resistance and easing the rolling process. A double-coated electrode with high mass loading was used to increase the diffraction statistics. A conventional organic electrolyte was employed instead of deuterated ones to reduce cost and evaluate whether high active-material loading could still yield acceptable data quality despite hydrogen background contributions.

3.2. Electrochemical comparison of different setups

The electrochemical performances of both setups were investigated by comparing their voltage profiles and differential capacity curves (Fig. 2).

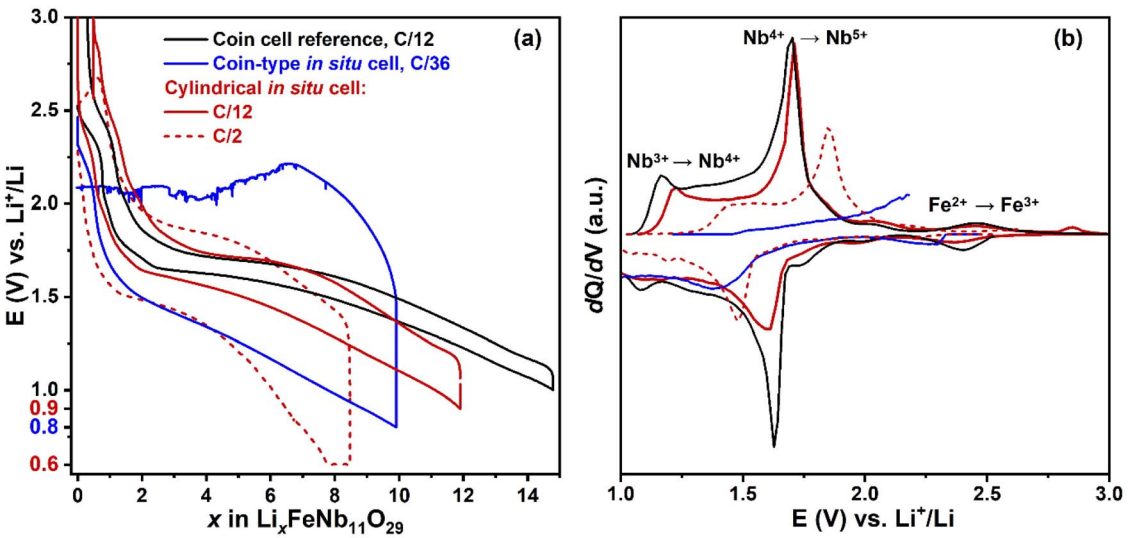

Fig. 2 Voltage profiles (a) and differential capacity curves (b) of $FeNb_{11}O_{29}$/Li half-cells in three different setups.

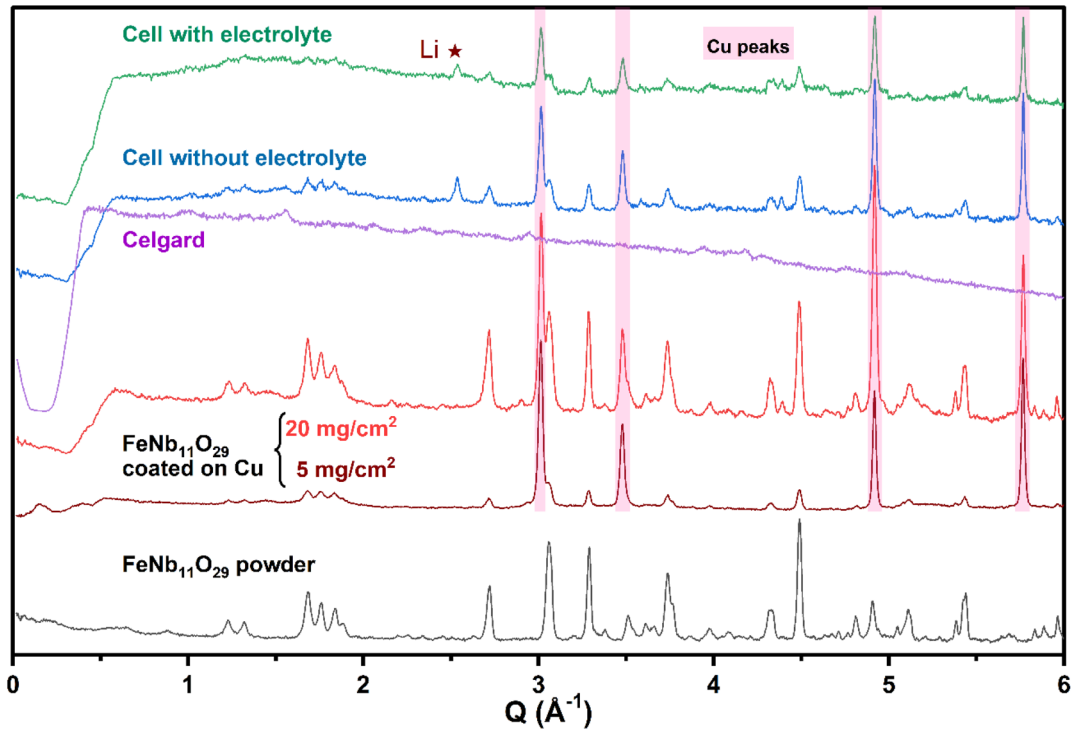

Fig. 3 Comparison of NPD patterns for $FeNb_{11}O_{29}$ powder, some components and the assembled cylindrical cell, obtained using the D2B diffractometer in 2 hours (except Celgard, measured using the D20 diffractometer in 5 minutes).

First, at the same current rate and comparable mass loading, the cylindrical and coin cells exhibit similar charge–discharge profiles with characteristic sloping features, consistent with dQ/dV peaks at ~2.4 V, 1.65 V, and 1.3 V, corresponding to $Fe^{3+/2+}$, $Nb^{5+/4+}$ and $Nb^{4+/3+}$ redox couples, respectively.[31–43] The cylindrical cell enables reversible cycling and delivers a capacity corresponding to ~12 Li^+ per formula unit (f.u.), lower than that of the coin cell (~15 Li^+ per f.u.). Its voltage profiles show higher polarisation and weaker dQ/dV peaks than the coin-cell reference, which could arise from local inhomogeneities at the rolled edges, slight variations in lithium thickness, and an imperfect compaction of the outermost layers of the jelly roll—effects that are difficult to eliminate completely by manual rolling. Despite these limitations, the cylindrical cell still exhibits modest polarisation (~200 mV) and low internal resistance (~1 Ω, Fig. S6). Increasing the rate to C/6 only led to a slight rise in polarisation and a minor capacity decrease, with approximately ~10 Li^+ exchanged (Fig. S7). Even at C/2, despite more pronounced polarization, the cell still accommodated ~8 Li^+, highlighting its impressive ability to endure high current while obtaining decent specific capacity. This electrochemical stability was still retained during prolonged cycling (Fig. S7). By contrast, the coin-type cell exhibits markedly poorer behaviour even at a much slower C/36 rate: a lower capacity of ~10 Li^+, large internal resistance (≈30–50 Ω), and subsequent voltage instability. These features could be due to unstable contact, electrolyte decomposition and parasitic reactions in the thick self-standing electrode.

3.3. Contribution of cylindrical cell components to data quality

To understand how the cylindrical cell design influences diffraction quality, the contribution of individual components was examined (Fig. 3).

For $FeNb_{11}O_{29}$ electrodes on copper foil (Fig. 3), the Cu reflections dominate the diffractograms regardless of the mass loading. However, with a loading of 20 mg cm^{-2}, the Bragg reflections of $FeNb_{11}O_{29}$ are significantly strong, comparable in intensity to that of the reference powder at both D2B and D20 beamlines, retaining well-defined peaks up to high Q. This demonstrates the critical role of mass loading in enhancing the signal-to-noise ratio of the active phase. At the D20 beamline, this high loading even allows fast data acquisitions in only five minutes (Fig. S8).

When the full stack (positive, negative, current collectors and separators) is placed inside the cylindrical cell without electrolyte, peak intensity and resolution of $FeNb_{11}O_{29}$ Bragg reflections decreased significantly, which could be due to incoherent scattering from the Celgard separator and strong absorption by the lithium foil. The influence of Celgard is clear in the diffractogram measured using D20, where it produces significant background signals. After electrolyte filling, the signal-to-noise ratio is slightly further worsened, since the peaks become less defined. Nevertheless, after careful background subtraction, the data quality remains sufficiently good for Rietveld refinement (Fig. S9 and Table S2), by including three phases, $FeNb_{11}O_{29}$, Cu and Li.

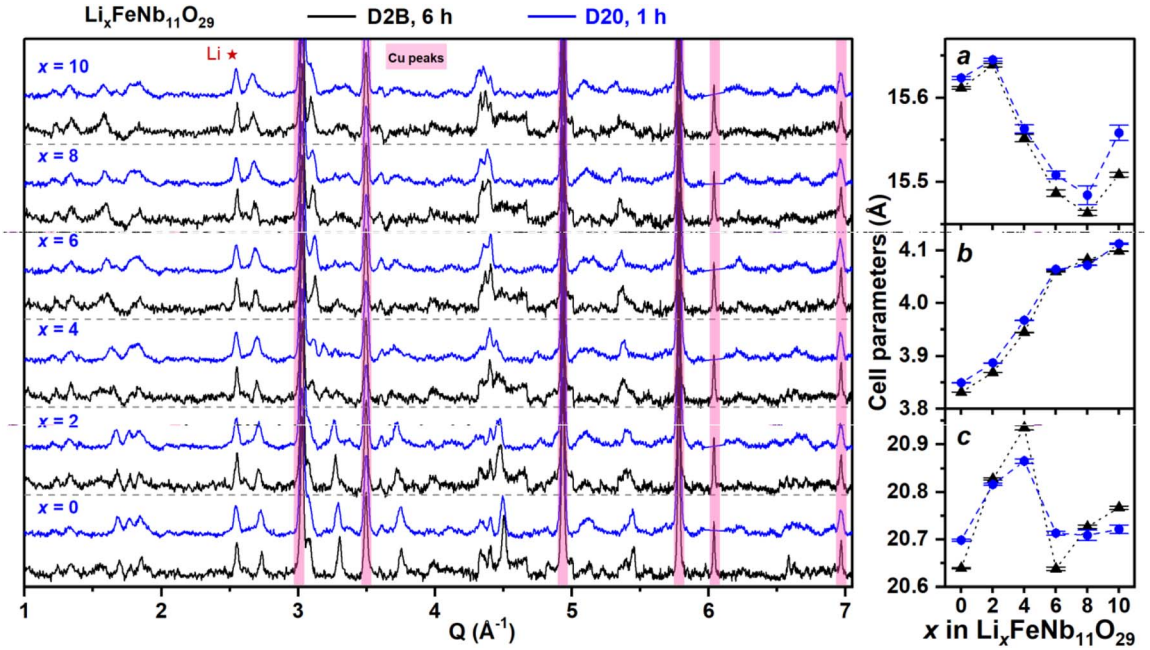

Fig. 4 NPD patterns of $Li_xFeNb_{11}O_{29}$ collected using D2B (6 h, black) and D20 (1 h, blue) diffractometers, and the corresponding Rietveld-refined cell parameters. The D2B diffractometer provides higher resolution, especially near $Q \approx 3$ Å^{-1} with better peak separation, while the D20 instrument offers a better signal-to-noise ratio.

These findings indicate that the conventional non-deuterated electrolyte is not the primary factor that decreases data quality; rather, the dominant contributions come from other cell components, notably the Celgard separator and the lithium foil. Importantly, a sufficiently high material mass—achieved by high areal loading on thin films—can compensate for these penalties and provide diffractograms of sufficient quality for structural analysis.

3.4. *Operando* NPD in cylindrical and coin-type cells

The comparison between NPD patterns of the cylindrical cell at several $Li_xFeNb_{11}O_{29}$ compositions, obtained using the two diffractometers, clarifies the instrumental characteristics (Fig. 4). For a given composition, both diffractometers recorded comparable peak positions and shapes, with closely similar cell parameters from Rietveld refinement. However, some differences between the two datasets could be observed. On the one hand, the patterns obtained using the D2B instrument show slightly better separation between $FeNb_{11}O_{29}$ reflections and Cu peaks, *e.g.* near $Q = 3$ Å^{-1}. This may come from (i) the intrinsic higher resolution of the D2B diffractometer or (ii) the phase relaxation and lithium homogenization within the electrode during 6 h of rest, evidenced by the noticeable potential equilibration (Fig. S7), making the peaks closer to a thermodynamically stable state. On the other hand, the D20 instrument with higher neutron flux enabled the collection of better signal-to-noise data in shorter time, although at the cost of slightly reduced peak resolution. The discrepancy in the *c* lattice parameter between the D2B and D20 likely arises from differences in relaxation time (6 h *vs.* 1 h) and the cycle number (1st *vs.* 2nd), which may influence structural relaxation and residual strain along the *c*-axis. Overall, these results confirmed that both instruments can deliver comparable structural information and the choice between them mainly depends on either the reaction kinetics to be probed or thermodynamics equilibrium.

Operando NPD of the cylindrical cell on the D20 reveals the structural changes of $FeNb_{11}O_{29}$ at three current rates, together with the electrochemical profiles (Fig. 5). During the initial C/12 discharge, continuous and progressive peak shifts are observed for many reflections, such as (011), (206), (020) and (420), indicating gradual lattice evolution as lithiation proceeds from $x = 0$ to $x = 11$. During the subsequent charge, the Bragg reflections shift back reversibly, with nearly all lithium extracted, and the structure returns close to its initial state. At higher rates (C/6 and C/2), this smooth peak shift behaviour is also seen, even though each five-minute acquisition corresponds to larger composition changes, making the patterns slightly less well-defined. Across three cycles, the absence of peak splitting or additional reflections is consistent with a single-phase, solid-solution mechanism. Besides, this demonstrates the robust structural reversibility of $FeNb_{11}O_{29}$ at fast cycling, which was also previously reported.[37,42] Overall, these results highlight the excellent capability of the cylindrical cell to support time-resolved measurements at high currents with good capacity retention.

Comparative analyses of *operando* NPD data obtained using cylindrical and coin-type cells help clarify the effect of cell designs on electrochemistry and diffraction data. Overall, the NPD patterns of each $Li_xFeNb_{11}O_{29}$ composition collected in two cells exhibit comparable peak positions for most reflections, indicating similar structural transitions and the

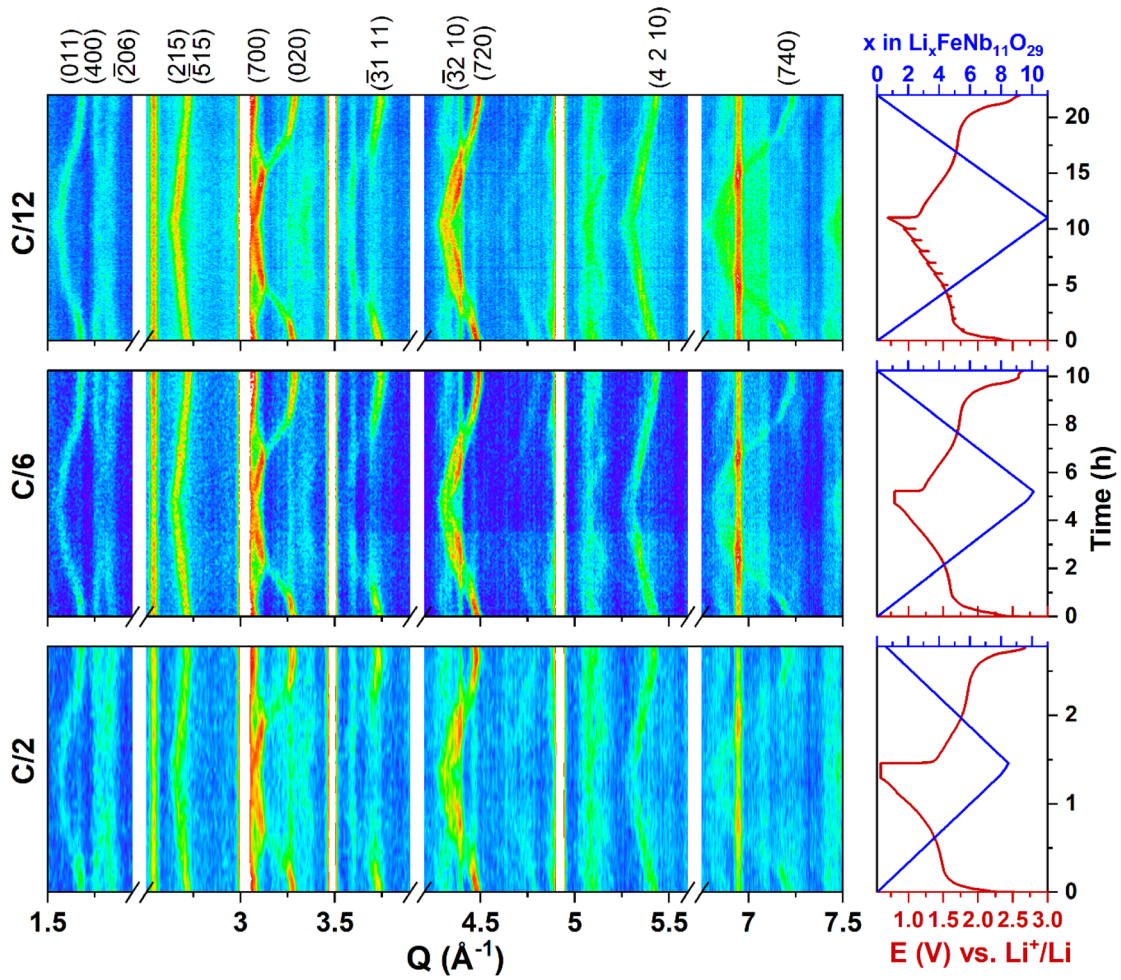

Fig. 5 *Operando* NPD contour plots of $Li_xFeNb_{11}O_{29}$ collected using the D20 diffractometer with 5-minute acquisitions during cycling at three current rates (C/12, C/6, and C/2), and the corresponding electrochemical profiles.

reliability of the cells (Fig. 6). However, differences could still be observed. For the cylindrical cell cycled at C/12, the contour plots exhibit clear, progressive peak shifts on discharge and a reversible evolution on charge, which are especially evident for the (0 1 1), (0 2 0), (4 2 0), (4 2 10), and (7 4 0) Bragg reflections (Fig. 5a), similar to the gradual and reversible peak evolutions in Fig. 6a. The slightly enhanced signal-to-noise ratio at C/6 may come from improved structural homogeneity after the initial C/12 cycle or reduced background scattering due to gravity-induced electrolyte movement in the vertically positioned cell. At C/2, rapid peak shifts during 5-minute acquisition broaden and weaken diffraction signals, lowering the resolution.

By contrast, analogous features are less evident for the coin-type cell cycled at C/36, both in the stacked patterns and in the contour plot (Fig. 6 and S10). First, while the peaks still evolve progressively during discharge, this behaviour becomes weaker or discontinuous at the end of charge, *e.g.* (0 2 0) reflection showing almost no shift and only a gradual, incomplete recovery of intensity. Additionally, the peak shape and intensity of $(\bar{3}\ 0\ 10)$ and (7 0 0) reflections remain nearly unchanged at the end of charge, indicating that the lithiated phase cannot be fully delithiated. After cycling, all reflections exhibit a clear decrease in intensity accompanied by a broadening of their full width at half maximum (FWHM, 2θ in degrees), which suggests the presence of several local lithiation states in the electrode. This could likely arise from the thick self-standing electrode, resulting in inhomogeneous electrochemical reactions and a lithium gradient within the electrode volume. This gradient in the lithiation degree, simplified as Li-rich and Li-poor contribution (Fig. 7), could reasonably explain the above observations: subtle peak evolution, incomplete intensity recovery and broadened FWHM at the end of charge. This interpretation is further supported by the contour plots (Fig. S10), where the shifts of some high-angle Bragg reflections, *e.g.* $(\overline{15}\ 1\ 5)$ and (7 4 0), while unambiguously observed for the cylindrical cell, are absent for the coin-type cell. These results highlight the impact of electrode configuration on data quality, with the cylindrical cell providing more homogeneous electrochemical reactions and, consequently, clearer structural evolution.

Besides the qualitative evaluation, further quantitative analyses allow the comparison of $FeNb_{11}O_{29}$ cell parameter

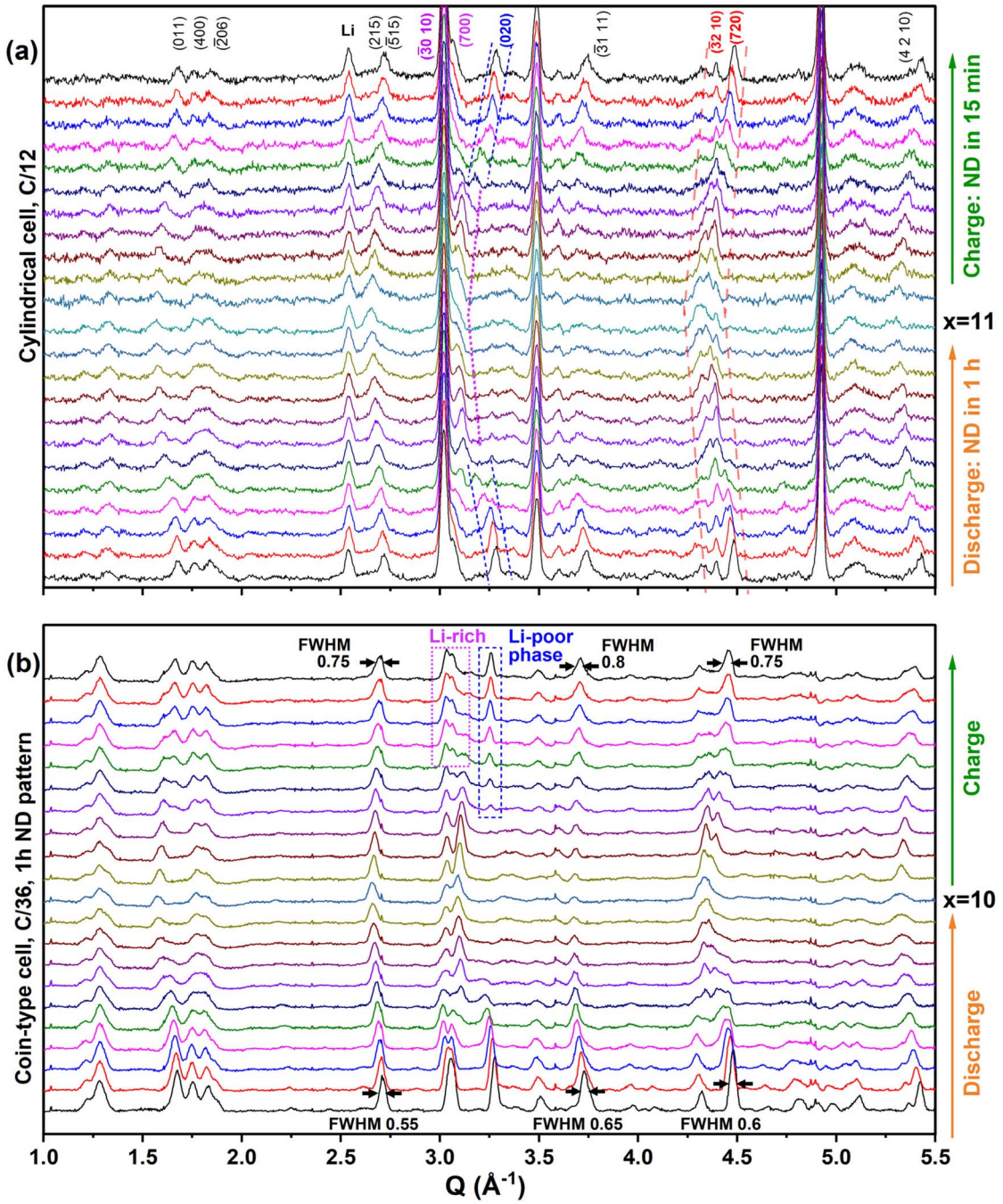

Fig. 6 Stacked NPD patterns ($Q = 1.0–5.5$ Å^{-1}) from *in situ*/*operando* experiments performed on the D20 diffractometer using (a) cylindrical and (b) coin-type cells, with full-width at half maximum (FWHM, 2θ in degrees) for some peaks. The cylindrical cell shows gradual, reversible peak shifts and intensity recovery, whereas the coin-type cell exhibits subtle peak evolution and reduced intensities at the end of charge.

evolution during *operando* NPD experiments in different setups (Fig. 7). For the cylindrical configuration, the cell parameters follow similar trends at the three applied current rates, with comparable standard uncertainties. This indicates that the structural changes of $FeNb_{11}O_{29}$ during lithiation and delithiation are largely independent of kinetics and demonstrated the excellent ability of the cell to sustain electrochemical reversibility at high currents. Compared with the reference data obtained from NPD in coin-type cells, the evolution trends were preserved, even though there were some discrepancies between the two setups. Such differences may come from experimental conditions, including electrode formulation, cycling rate, and, most critically, mass loading and electrode thickness (~0.2 mm for the cylindrical cell *versus* ~1 mm for the coin-type cell). Thicker electrodes are more likely to cause inhomogeneous lithium insertion/extraction across the electrode depth, which may take more time to homogenize and lead to the lattice parameter differences in the two cells. Despite these

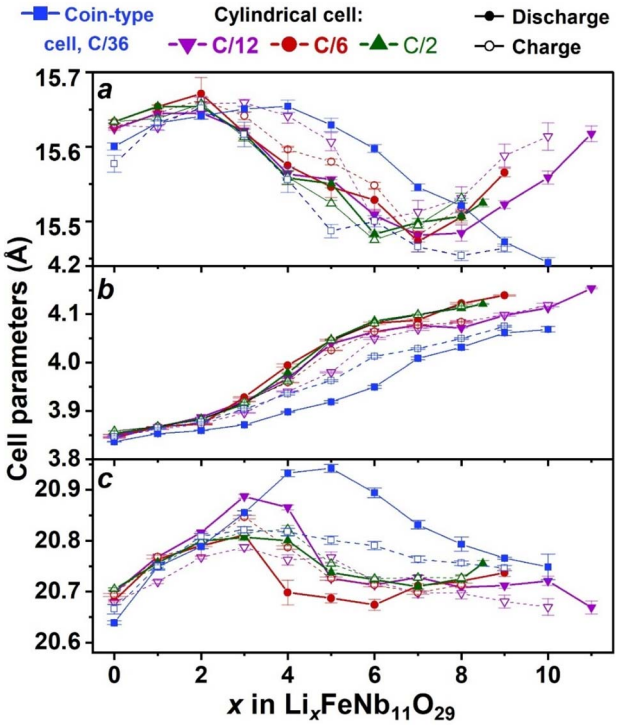

Fig. 7 Evolution of $FeNb_{11}O_{29}$ cell parameters obtained from Rietveld refinement of *operando* NPD data obtained using the D20 diffractometer in cylindrical and coin-type cells. Error bars indicate the standard uncertainties of the refined parameters.

discrepancies, the general agreement across the three datasets highlights the reliability of cylindrical cells for *operando* neutron diffraction studies.

Finally, post-cycling analyses were conducted to probe the spatial homogeneity of the cylindrical cell. Vertical NPD scans on the D20 diffractometer using a 1 cm slit at several positions along the electrode height show the characteristic $FeNb_{11}O_{29}$ reflections at the same 2θ positions across all sections (Fig. S11). The signal-to-noise ratio is lower due to the reduced probed volume, but no shift or broadening indicative of a vertical gradient is observed. Complementary XRD measurements were performed on punched electrodes from different radial and axial positions of the rolled electrode, revealing nearly identical peak positions and only minor fluctuations in refined lattice parameters (Fig. S12). Overall, these results confirm that the jelly roll built from thin, double-coated layers provides uniform contact and pressure, enabling homogeneous reactions throughout the cell.

4. Conclusions

In this study, we have benchmarked *operando* neutron powder diffraction by comparing the cell configurations and high-flux or high-resolution diffractometers. The results reveal complementary characteristics for each setup, offering practical design guidelines for *operando* NPD in battery research.

Coin-type cells are suitable for preliminary investigations, particularly when material availability is limited and fast-charging conditions are not required. Their hydrogen-free components ensure excellent signal-to-noise ratios. They allow the use of self-standing electrodes and small volumes of deuterated electrolytes, which minimizes background scattering and avoids peak overlap, further enhancing diffraction pattern quality. However, thick electrodes can introduce inhomogeneities, high resistance, polarization, and a limited cycling rate. Regarding practicability, their simple assembly facilitates troubleshooting during beamtime, making them a pragmatic choice for foundational studies before more extensive studies using cylindrical cells, if necessary.

Cylindrical cells, on the other hand, are better suited for high-rate cycling studies (*e.g.*, fast-charging materials or kinetic effects on structural evolutions) and cost-effective experiments, as they allow the use of conventional organic electrolytes. This configuration closely mimics that of commercial large-format cells (*e.g.*, 18650), providing realistic operating conditions for upscaling and commercialization studies. While cylindrical cells introduce additional background contributions, careful background subtraction ensures data quality sufficient for structural refinements. Their ability to accommodate double-coated thin films enables (i) sufficient counting statistics, (ii) homogeneous electrochemistry, and (iii) rapid NPD acquisitions (as fast as 5 minutes) and cycling rates up to C/2. These advantages were reflected in this work, where the *operando* results confirmed the solid-solution mechanism of $FeNb_{11}O_{29}$ as previously reported, while also demonstrating structural reversibility even at high-rate cycling, rate-induced peak broadening, and challenges associated with Li localization and occupancies in the Wadsley–Roth family.

Looking forward, these findings open perspectives for performing *operando* neutron powder diffraction, a more accessible and routine tool in battery research. The cylindrical cell represents a promising tool for balancing realistic electrochemistry with sufficiently good data quality, especially for investigating high-rate electrode materials by NPD. The cell design could be further optimized by reducing parasitic scattering and absorption—for example, using thinner lithium foil, alternative separators with reduced background, alternative neutron-transparent current collectors (V or a $Ti_{2.08}Zr$ alloy), partially deuterated electrolyte, or highly crystalline active materials. While each of these strategies can improve data quality, their combined effects on the overall signal-to-noise ratio require further investigation to reach a compromise between applicability and data quality, as these effects depend on the interplay of all cell components. For example, even slight reductions in lithium foil thickness can significantly mitigate neutron absorption, but the overall improvement is affected by the separator, current collector, and electrolyte. Besides, using enriched ^{7}Li foil could theoretically be a strategy to reduce neutron absorption, but its implementation is challenging due to negligible improvement in coherent scattering compared with the ^{6}Li isotope, its high cost, no commercial availability, and the need for extensive validation with ^{7}Li-enriched electrolyte. On the instrumentation side, the combined use of the D2B and D20 diffractometers can offer both high-resolution

structural details and time-resolved insights, providing comprehensive information on electrochemical reactions.

Author contributions

D. Le Thanh: data curation, formal analysis, writing – original draft. C. Villevieille: methodology, resources, writing – review & editing. E. Suard: data curation, supervision, writing – review & editing. R. Berthelot: supervision, conceptualization, writing – review & editing. All the authors have read and approved the final version of the manuscript.

Conflicts of interest

There are no conflicts to declare.

Data availability

The data supporting this article have been included as part of the supplementary information (SI). Neutron diffraction data collected at the ILL are available at https://doi.org/10.5291/ILL-DATA.5-21-1198; https://doi.org/10.5291/ILL-DATA.5-23-831; https://doi.org/10.5291/ILL-DATA.5-24-713.

Supplementary information is available. See DOI: https://doi.org/10.1039/d5ta10422j.

Acknowledgements

As a part of the DESTINY PhD program, this publication was funded by the European Union's Horizon 2020 research and innovation program under the Marie Skłodowska-Curie Actions COFUND (Grant Agreement #945357). R. B. acknowledges the French National Research Agency (STORE-EX Labex Project ANR-10-LABX-76-01).

References

1 J. B. Goodenough and K.-S. Park, The Li-Ion Rechargeable Battery: A Perspective, *J. Am. Chem. Soc.*, 2013, **135**, 1167–1176, DOI: 10.1021/ja3091438.

2 L. Croguennec and M. R. Palacin, Recent Achievements on Inorganic Electrode Materials for Lithium-Ion Batteries, *J. Am. Chem. Soc.*, 2015, **137**, 3140–3156, DOI: 10.1021/ja507828x.

3 D. Larcher and J.-M. Tarascon, Towards greener and more sustainable batteries for electrical energy storage, *Nat. Chem.*, 2015, **7**, 19–29, DOI: 10.1038/nchem.2085.

4 A. Manthiram, An Outlook on Lithium Ion Battery Technology, *ACS Cent. Sci.*, 2017, **3**, 1063–1069, DOI: 10.1021/acscentsci.7b00288.

5 T. Kim, W. Song, D.-Y. Son, L. K. Ono and Y. Qi, Lithium-ion batteries: outlook on present, future, and hybridized technologies, *J. Mater. Chem. A*, 2019, **7**, 2942–2964, DOI: 10.1039/C8TA10513H.

6 A. Manthiram, A reflection on lithium-ion battery cathode chemistry, *Nat. Commun.*, 2020, **11**, 1550, DOI: 10.1038/s41467-020-15355-0.

7 Ö. Bergström, A. M. Andersson, K. Edström and T. Gustafsson, A neutron diffraction cell for studying lithium-insertion processes in electrode materials, *J. Appl. Crystallogr.*, 1998, **31**, 823–825, DOI: 10.1107/S002188989800538X.

8 H. Berg, H. Rundlöv and J. O. Thomas, The $LiMn_2O_4$ to λ-MnO_2 phase transition studied by in situ neutron diffraction, *Solid State Ionics*, 2001, **144**, 65–69, DOI: 10.1016/S0167-2738(01)00894-3.

9 W. K. Pang and V. K. Peterson, A custom battery for operando neutron powder diffraction studies of electrode structure, *J. Appl. Crystallogr.*, 2015, **48**, 280–290, DOI: 10.1107/S1600576715000679.

10 W. K. Pang, N. Sharma, V. K. Peterson, J.-J. Shiu and S. Wu, In-situ neutron diffraction study of the simultaneous structural evolution of a $LiNi_{0.5}Mn_{1.5}O_4$ cathode and a $Li_4Ti_5O_{0.12}$ anode in a $LiNi_{0.5}Mn_{1.5}O_4||Li_4Ti_5O_{0.12}$ full cell, *J. Power Sources*, 2014, **246**, 464–472, DOI: 10.1016/j.jpowsour.2013.07.114.

11 W. K. Pang, S. Kalluri, V. K. Peterson, S. X. Dou and Z. Guo, Electrochemistry and structure of the cobalt-free $Li_{1+x}MO_2$ (M = Li, Ni, Mn, Fe) composite cathode, *Phys. Chem. Chem. Phys.*, 2014, **16**, 25377–25385, DOI: 10.1039/C4CP02864C.

12 W. K. Pang, M. Alam, V. K. Peterson and N. Sharma, Structural evolution of electrodes in the NCR and CGR cathode-containing commercial lithium-ion batteries cycled between 3.0 and 4.5 V: an operando neutron powder-diffraction study, *J. Mater. Res.*, 2015, **30**, 373–380, DOI: 10.1557/jmr.2014.297.

13 J. J. Biendicho, M. Roberts, C. Offer, D. Noréus, E. Widenkvist, R. I. Smith, G. Svensson, K. Edström, S. T. Norberg, S. G. Eriksson and S. Hull, New in-situ neutron diffraction cell for electrode materials, *J. Power Sources*, 2014, **248**, 900–904, DOI: 10.1016/j.jpowsour.2013.09.141.

14 X.-L. Wang, K. An, L. Cai, Z. Feng, S. E. Nagler, C. Daniel, K. J. Rhodes, A. D. Stoica, H. D. Skorpenske, C. Liang, W. Zhang, J. Kim, Y. Qi and S. J. Harris, Visualizing the chemistry and structure dynamics in lithium-ion batteries by in-situ neutron diffraction, *Sci. Rep.*, 2012, **2**, 747, DOI: 10.1038/srep00747.

15 B. Vadlamani, K. An, M. Jagannathan and K. S. R. Chandran, An In-Situ Electrochemical Cell for Neutron Diffraction Studies of Phase Transitions in Small Volume Electrodes of Li-Ion Batteries, *J. Electrochem. Soc.*, 2014, **161**, A1731–A1741, DOI: 10.1149/2.0951410jes.

16 B. Song, G. M. Veith, J. Park, M. Yoon, P. S. Whitfield, M. J. Kirkham, J. Liu and A. Huq, Metastable $Li_{1+\delta}Mn_2O_4$ ($0 \leq \delta \leq 1$) Spinel Phases Revealed by in Operando Neutron Diffraction and First-Principles Calculations, *Chem. Mater.*, 2019, **31**, 124–134, DOI: 10.1021/acs.chemmater.8b03199.

17 P.-H. Chien, X. Wu, B. Song, Z. Yang, C. K. Waters, M. S. Everett, F. Lin, Z. Du and J. Liu, New Insights into Structural Evolution of $LiNiO_2$ Revealed by Operando

Neutron Diffraction, *Batteries Supercaps*, 2021, **4**, 1701–1707, DOI: 10.1002/batt.202100135.

18 F. Rosciano, M. Holzapfel, W. Scheifele and P. Novák, A novel electrochemical cell for *in situ* neutron diffraction studies of electrode materials for lithium-ion batteries, *J. Appl. Crystallogr.*, 2008, **41**, 690–694, DOI: 10.1107/S0021889808018025.

19 J.-F. Colin, V. Godbole and P. Novák, *In situ* neutron diffraction study of Li insertion in $Li_4Ti_5O_{12}$, *Electrochem. Commun.*, 2010, **12**, 804–807, DOI: 10.1016/j.elecom.2010.03.038.

20 V. Godbole, M. Hess, C. Villevieille, H. Kaiser, J.-F. Colin and P. Novak, Circular in situ neutron powder diffraction cell for study of reaction mechanism in electrode materials for Li-ion batteries, *RSC Adv.*, 2013, **3**, 757–763, DOI: 10.1039/C2RA21526H.

21 M. Bianchini, J. B. Leriche, J.-L. Laborier, L. Gendrin, E. Suard, L. Croguennec and C. Masquelier, A New Null Matrix Electrochemical Cell for Rietveld Refinements of In-Situ or Operando Neutron Powder Diffraction Data, *J. Electrochem. Soc.*, 2013, **160**, A2176–A2183, DOI: 10.1149/2.076311jes.

22 N. Sharma, G. Du, A. J. Studer, Z. Guo and V. K. Peterson, In-situ neutron diffraction study of the MoS_2 anode using a custom-built Li-ion battery, *Solid State Ionics*, 2011, **199–200**, 37–43, DOI: 10.1016/j.ssi.2011.07.015.

23 N. Sharma, M. V. Reddy, G. Du, S. Adams, B. V. R. Chowdari, Z. Guo and V. K. Peterson, Time-Dependent in-Situ Neutron Diffraction Investigation of a $Li(Co_{0.16}Mn_{1.84})O_4$ Cathode, *J. Phys. Chem. C*, 2011, **115**, 21473–21480, DOI: 10.1021/jp2026237.

24 W. R. Brant, S. Schmid, G. Du, H. E. A. Brand, W. K. Pang, V. K. Peterson, Z. Guo and N. Sharma, In Situ Neutron Powder Diffraction Using Custom-made Lithium-ion Batteries, *JoVE*, 2014, 52284, DOI: 10.3791/52284.

25 G. Du, N. Sharma, V. K. Peterson, J. A. Kimpton, D. Jia and Z. Guo, Br-Doped $Li_4Ti_5O_{12}$ and Composite TiO_2 Anodes for Li-ion Batteries: Synchrotron X-Ray and In Situ Neutron Diffraction Studies, *Adv. Funct. Mater.*, 2011, **21**, 3990–3997, DOI: 10.1002/adfm.201100846.

26 M. Roberts, J. J. Biendicho, S. Hull, P. Beran, T. Gustafsson, G. Svensson and K. Edström, Design of a new lithium ion battery test cell for in-situ neutron diffraction measurements, *J. Power Sources*, 2013, **226**, 249–255, DOI: 10.1016/j.jpowsour.2012.10.085.

27 L. Boulet-Roblin, P. Borel, D. Sheptyakov, C. Tessier, P. Novák and C. Villevieille, Operando Neutron Powder Diffraction Using Cylindrical Cell Design: The Case of $LiNi_{0.5}Mn_{1.5}O_4$ vs. Graphite, *J. Phys. Chem. C*, 2016, **120**, 17268–17273, DOI: 10.1021/acs.jpcc.6b05777.

28 D. Sheptyakov, L. Boulet-Roblin, V. Pomjakushin, P. Borel, C. Tessier and C. Villevieille, Stroboscopic neutron diffraction applied to fast time-resolved *operando* studies on Li-ion batteries (d-$LiNi_{0.5}Mn_{1.5}O_4$ *vs.* graphite), *J. Mater. Chem. A*, 2020, **8**, 1288–1297, DOI: 10.1039/C9TA11826H.

29 L. Vitoux, M. Reichardt, S. Sallard, P. Novák, D. Sheptyakov and C. Villevieille, A Cylindrical Cell for Operando Neutron Diffraction of Li-Ion Battery Electrode Materials, *Front. Energy Res.*, 2018, **6**, 76, DOI: 10.3389/fenrg.2018.00076.

30 A. V. Dobromyslov and N. I. Taluts, Structure studies of quenched and tempered Zr-Ti alloys, *Fiz. Met. Metalloved.*, 1987, **63**(1), 127–132.

31 X. Lou, C. Lin, Q. Luo, J. Zhao, B. Wang, J. Li, Q. Shao, X. Guo, N. Wang and Z. Guo, Crystal Structure Modification Enhanced $FeNb_{11}O_{29}$ Anodes for Lithium-Ion Batteries, *ChemElectroChem*, 2017, **4**, 3171–3180, DOI: 10.1002/celc.201700816.

32 D. Spada, M. C. Mozzati, B. Albini, P. Galinetto, I. Quinzeni, D. Capsoni and M. Bini, Deepening the shear structure $FeNb_{11}O_{29}$: influence of polymorphism and doping on structural, spectroscopic and magnetic properties, *Dalton Trans.*, 2018, **47**, 15816–15826, DOI: 10.1039/C8DT02896F.

33 R. Zheng, S. Qian, X. Cheng, H. Yu, N. Peng, T. Liu, J. Zhang, M. Xia, H. Zhu and J. Shu, $FeNb_{11}O_{29}$ nanotubes: superior electrochemical energy storage performance and operating mechanism, *Nano Energy*, 2019, **58**, 399–409, DOI: 10.1016/j.nanoen.2019.01.065.

34 D. Spada, B. Albini, P. Galinetto, D. Versaci, C. Francia, S. Bodoardo, G. Bais and M. Bini, $FeNb_{11}O_{29}$, anode material for high-power lithium-ion batteries: pseudocapacitance and symmetrisation unravelled with advanced electrochemical and in situ/operando techniques, *Electrochim. Acta*, 2021, **393**, 139077, DOI: 10.1016/j.electacta.2021.139077.

35 D. Spada, I. Quinzeni and M. Bini, Orthorhombic and monoclinic modifications of $FeNb_{11}O_{29}$, as promising anode materials for lithium batteries: relationships between pseudocapacitive behaviour and structure, *Electrochim. Acta*, 2019, **296**, 938–944, DOI: 10.1016/j.electacta.2018.11.047.

36 M. Bini, I. Quinzeni and D. Spada, The Doping of $FeNb_{11}O_{29}$ as a Way to Improve Its Electrochemical Performances, *ChemistrySelect*, 2019, **4**, 5656–5661, DOI: 10.1002/slct.201901182.

37 Y. Yang, H. Zhu, F. Yang, F. Yang, D. Chen, Z. Wen, D. Wu, M. Ye, Y. Zhang, J. Zhao, Q. Liu, X. Lu, M. Gu, C. C. Li and W. He, Ten Thousand-Cycle Ultrafast Energy Storage of Wadsley–Roth Phase Fe–Nb Oxides with a Desolvation Promoting Interfacial Layer, *Nano Lett.*, 2021, **21**, 9675–9683, DOI: 10.1021/acs.nanolett.1c03478.

38 Z. Lv, H. Zhu, W. Meng, L. Wei, Y. Yang, Y. Zhang, M. Ye and C. C. Li, Cation mixing in Wadsley-Roth phase anode of lithium-ion battery improves cycling stability and fast Li^+ storage, *Applied Physics Reviews*, 2021, **8**, 031404, DOI: 10.1063/5.0054030.

39 Y. Yang and J. Zhao, Wadsley–Roth Crystallographic Shear Structure Niobium-Based Oxides: Promising Anode Materials for High-Safety Lithium-Ion Batteries, *Advanced Science*, 2021, **8**, 2004855, DOI: 10.1002/advs.202004855.

40 J. Huang, Q. Chen, S. Chen, L. Luo, J. Li, C. Lin and Y. Chen, Al^{3+}-doped $FeNb_{11}O_{29}$ anode materials with enhanced lithium-storage performance, *Adv. Compos. Hybrid Mater.*, 2021, **4**, 733–742, DOI: 10.1007/s42114-021-00291-4.

41 H. Fu, Y. Lian, Y. Bai, Z. Wang, Y. Hu, J. Zhao and H. Zhang, Porous biscuit-like nanoplate $FeNb_{11}O_{29-x}$@C for lithium-ion storage and oxygen evolution, *Nanoscale*, 2022, **14**, 17428–17437, DOI: 10.1039/D2NR05020J.

42 D. Le Thanh, A. Guiet, E. Suard and R. Berthelot, Downsizing $FeNb_{11}O_{29}$ anode material through ultrafast solid-state microwave-assisted synthesis for enhanced electrochemical performance, *J. Solid State Chem.*, 2024, **330**, 124444, DOI: 10.1016/j.jssc.2023.124444.

43 M. Bini, $FeNb_{11}O_{29}$ and related niobate anodes for fast-charging lithium-ion batteries: a review, *J. Solid State Electrochem.*, 2025, **29**, 4101–4116, DOI: 10.1007/s10008-024-05847-0.

44 J. Rodriguez-Carvajal, Recent developments of the program FULLPROF, commission on powder diffraction, *IUCr Newsl.*, 2001, **26**, 12–19.

45 I. Pinus, M. Catti, R. Ruffo, M. M. Salamone and C. M. Mari, Neutron Diffraction and Electrochemical Study of $FeNb_{11}O_{29}$/$Li_{11}FeNb_{11}O_{29}$ for Lithium Battery Anode Applications, *Chem. Mater.*, 2014, **26**, 2203–2209, DOI: 10.1021/cm500442j.